



First [N II]122 μm Line Detection in a QSO-SMG Pair BRI 1202–0725 at $z = 4.69$

Minju M. Lee^{1,2,3}, Tohru Nagao⁴, Carlos De Breuck⁵, Stefano Carniani⁶, Giovanni Cresci⁷, Bunyo Hatsukade⁸, Ryohei Kawabe^{9,10,11}, Kotaro Kohno^{8,12}, Roberto Maiolino^{13,14}, Filippo Mannucci⁷, Alessandro Marconi^{7,15}, Kouichiro Nakanishi^{3,10}, Toshiki Saito¹⁶, Yoichi Tamura², Paulina Troncoso¹⁷, Hideki Umehata^{8,18}, and Min Yun¹⁹

¹Max-Planck-Institut für Extraterrestrische Physik (MPE), Giessenbachstr., D-85748 Garching, Germany; minju@mpe.mpg.de

²Division of Particle and Astrophysical Science, Graduate School of Science, Nagoya University, Furo-cho, Chikusa-ku, Nagoya 464-8602, Japan

³National Observatory of Japan, 2-21-1 Osawa, Mitaka, Tokyo 181-8588, Japan

⁴Research Center for Space and Cosmic Evolution, Ehime University, 2-5 Bunkyo-cho, Matsuyama 790-8577, Japan

⁵European Southern Observatory, Karl Schwarzschild Straße 2, D-85748 Garching, Germany

⁶Scuola Normale Superiore, Piazza dei Cavalieri 7, I-56126 Pisa, Italy

⁷INAF—Osservatorio Astrofisico di Arcetri, Largo E. Fermi 5, I-20125 Firenze, Italy

⁸Institute of Astronomy, Graduate School of Science, The University of Tokyo, 2-21-1 Osawa, Mitaka, Tokyo 181-0015, Japan

⁹National Astronomical Observatory of Japan, 2-21-1 Osawa, Mitaka, Tokyo 181-8588, Japan

¹⁰SOBENDAI (The Graduate University for Advanced Studies), 2-21-1 Osawa, Mitaka, Tokyo 181-8588, Japan

¹¹Department of Astronomy, The University of Tokyo, 7-3-1 Hongo, Bunkyo-ku, Tokyo 113-0033, Japan

¹²Research Center for the Early Universe, The University of Tokyo, 7-3-1 Hongo, Bunkyo, Tokyo 113-0033, Japan

¹³Cavendish Laboratory, University of Cambridge, 19 J. J. Thomson Avenue, Cambridge CB3 0HE, UK

¹⁴Kavli Institute for Cosmology, University of Cambridge, Madingley Road, Cambridge CB3 0HA, UK

¹⁵Dipartimento di Fisica e Astronomia, Università degli Studi di Firenze, Via G. Sansone 1, I-50019 Sesto F.no, Firenze, Italy

¹⁶Max-Planck Institute for Astronomy, Königstuhl, 17 D-69117 Heidelberg, Germany

¹⁷Universidad Autónoma de Chile, Chile, Av. Pedro de Valdivia 425, Providencia, Santiago de Chile, Chile

¹⁸RIKEN Cluster for Pioneering Research, 2-1 Hirosawa, Wako, Saitama 351-0198, Japan

¹⁹Department of Astronomy, University of Massachusetts, Amherst, MA 01003, USA

Received 2019 April 17; revised 2019 September 3; accepted 2019 September 3; published 2019 September 24

Abstract

We report the first detection obtained with the Atacama Large Millimeter/submillimeter Array of the [N II] 122 μm line emission from a galaxy group BRI 1202–0725 at $z = 4.69$ consisting of a quasi-stellar object (QSO) and a submillimeter-bright galaxy (SMG). Combining this with a detection of [N II] 205 μm line in both galaxies, we constrain the electron densities of the ionized gas based on the line ratio of [N II] 122/205. The derived electron densities are 26_{-11}^{+12} and 134_{-39}^{+50} cm^{-3} for the SMG and the QSO, respectively. The electron density of the SMG is similar to that of the Galactic Plane and to the average of the local spirals. However, higher electron densities (by up to a factor of three) could be possible for systematic uncertainties of the line flux estimates. The electron density of the QSO is comparable to high- z star-forming galaxies at $z = 1.5$ – 2.3 , obtained using rest-frame optical lines and with the lower limits suggested from stacking analysis on lensed starbursts at $z = 1$ – 3.6 using the same tracer of [N II]. Our results suggest a large scatter of electron densities in global scale at fixed star formation rates for extreme starbursts. The success of the [N II] 122 μm and 205 μm detections at $z = 4.69$ demonstrates the power of future systematic surveys of extreme starbursts at $z > 4$ for probing the interstellar medium conditions and the effects on surrounding environments.

Key words: galaxies: evolution – galaxies: high-redshift – galaxies: ISM – galaxies: starburst – quasars: general – submillimeter: galaxies

1. Introduction

Understanding the physical conditions of star formation is critical in constraining theoretical models of galaxy evolution. Galaxies form stars at a higher rate in the early universe at a fixed mass. A subsequent question is how the interstellar medium (ISM) properties are correspondingly changed to understand the cosmic evolution. Observations of $z > 1$ star-forming galaxies suggest that the ISM state and/or the hardness of the extreme ultraviolet (EUV) radiation field were more extreme in the past than in the present day. For example, rest-frame optical line observations revealed that electron densities of high-redshift star-forming galaxies range between 100 and 1000 cm^{-3} , which is up to two orders of magnitude higher than those observed in the local universe (e.g., Masters et al. 2014; Steidel et al. 2014; Sanders et al. 2016; Kaasinen et al. 2017).

Far-infrared (FIR) transitions are a powerful tool for investigating the ISM. The fact that they are less affected by dust compared to optical line tracers makes them highly

advantageous for probing dusty star-forming galaxies. At wavelengths greater than 100 μm , the fine-structure transitions of [C II] 157.7 μm , the [N II] 121.9, and 205.2 μm have been used for probing ISM conditions of local and high- z galaxies (Stacey et al. 1991; Wright et al. 1991; Bennett et al. 1994; Lord et al. 1996; Malhotra et al. 2001; Brauher et al. 2008; Nagao et al. 2012; Farrah et al. 2013; Zhao et al. 2013, 2016a, 2016b; Herrera-Camus et al. 2016, 2018a, 2018b). With an ionization threshold of 11.3 eV, the [C II] line emission arises from the neutral and the ionized gas. On the other hand, the two [N II] fine-structure lines originate from fully ionized gas because the ionization potential of nitrogen (14.5 eV) is about ~ 0.9 eV higher than that of hydrogen. Therefore, the ionized nitrogen [N II] lines reflect the effect of UV photons emitted by massive young stars, with possible enhancement from X-ray photoionization. The combination of two fine-structure lines can be used as a tracer of electron density and this diagnostic barely depends on the electron temperature (e.g., Goldsmith et al. 2015; Herrera-Camus et al. 2016).

The [N II] 122 μm line emission has not been detected for galaxies at $4 < z < 7$ until now, which is the epoch when larger number of galaxies are beginning to form after the end of the reionization. In this Letter, we report the first detection of [N II] 122 μm line from a quasi-stellar object (QSO)-submillimeter-bright galaxy (SMG) pair, BRI 1202–0725, at $z = 4.69$. This compact group of BRI 1202–0725 was one of the first $z > 4$ submillimeter-bright systems discovered (Isaak et al. 1994) and remains the archetype for major starbursts in gas-rich mergers in the early universe. It consists of an optically selected QSO, an optically faint SMG that is located $4''$ (≈ 26 kpc) northwest of the quasar (Hu et al. 1996; Omont et al. 1996), and two Ly α -selected galaxies in their very vicinity (Fontana et al. 1996; Hu et al. 1996; Ohta et al. 2000; Salomé et al. 2012; Carilli et al. 2013; Carniani et al. 2013). Extremely high FIR luminosities of QSOs and SMGs (Omont et al. 1996; Yun et al. 2000; Iono et al. 2006; $\sim 10^{13} L_{\odot}$) imply vigorous star-forming activity of $\approx 1000 M_{\odot} \text{ yr}^{-1}$. The system is known to have rich C-bearing emission line data sets; various rotational CO molecular lines have been detected to up $J = 11$ (e.g., Ohta et al. 1996; Omont et al. 1996; Salomé et al. 2012) in addition to bright [C II] emissions (Iono et al. 2006; Carilli et al. 2013). Lu et al. (2017; hereafter, Lu17) reported the first detection of [N II] 205 μm line emissions for both systems and measured the dust temperature ($T_{\text{dust}} = 43 \pm 2$ K) using the line ratio between the [N II] line and CO (7–6). We add new [N II] 122 μm line detections, which provide further constraints on the physical conditions of the ISM, namely the electron density.

We assume $H_0 = 67.8 \text{ km s}^{-1} \text{ Mpc}^{-1}$, $\Omega_0 = 0.308$ and $\Omega_{\Lambda} = 0.692$ (Planck Collaboration et al. 2015).

2. Atacama Large Millimeter/submillimeter Array (ALMA) Observations and Data Reduction

2.1. Band 6 Observations for [N II] 205 μm

The Band 6 observations were carried out for our ALMA Cycle 2 program. A total of 39 and 40 antennas were used with the unprojected length (L_{baseline}) between 15 and 348 m (C34-2/1) on 2014 December 14 and 2015 January 4 with a total on-source time of 58 minutes.

We used four spectral windows (SPWs), each being 1.875 GHz wide. Two of them were set in the upper sideband with 3.906 MHz resolution ($\sim 4.5 \text{ km s}^{-1}$) to target [N II] 205 μm . One SPW in the lower sideband was also set to 3.906 MHz resolution. The remaining SPW was set to 7.812 MHz resolution ($\sim 9.7 \text{ km s}^{-1}$), in which we detected CO (12–11) emissions both from the SMG and the QSO (M. Lee et al. 2019, in preparation). Two strong quasars J1256–0547 and J1058+0133 were chosen for bandpass calibration. J1216–1033 was the phase calibrator. Callisto was the flux calibrator.

2.2. Band 8 Observations for [N II] 122 μm

The Band 8 observations at 700 μm were also a subset of the same ALMA Cycle 2 program. Observations used 37 or 38 antennas with the unprojected length (L_{baseline}) between 21 and 783 m on 2015 June 6 through 8 and total on-source time was 112 minutes.

We used four SPWs, each being 1.875 GHz wide. Two of them were set in the upper sideband with 3.906 MHz resolution ($\sim 2.7 \text{ km s}^{-1}$) to detect [N II] 122 μm . The spectral resolution for the remaining two SPWs in the lower sideband was set to

7.812 MHz ($\sim 5.6 \text{ km s}^{-1}$). J1256–0547 was chosen as a bandpass and a phase calibrator. 3C 273 and Titan were chosen for flux calibrators.

2.3. Archival Data: Band 6 Archival Data

We downloaded the archival data sets that were independently taken during ALMA Cycle 3 for [N II] 205 μm line detection reported in Lu17. The details of the observations are presented in Lu17. We calibrated the data based on the provided pipeline script. It was observed in the time-domain mode (TDM) with a spectral resolution of 15.625 MHz, corresponding to $\sim 19 \text{ km s}^{-1}$, in which the spectral sampling is a factor of ≈ 4 coarser than our Band 6 data sets. Hereafter, we will refer the data as the “Lu data.”

2.4. Data Reduction and Analysis

We performed calibration using the Common Astronomy Software Applications package (CASA; McMullin et al. 2007). For our Band 6 and 8 data sets, we used the calibration scripts provided by the ALMA ARC members that used CASA version of 4.2.2 and 4.3.1, respectively. For the Lu data, we used CASA 4.5.2.

Images were produced by CASA task `tclean`. All imaging processes were handled with the 5.4.0 version. Using the natural weighting, the synthesized beam sizes are $1''.43 \times 0''.84$ and $0''.32 \times 0''.24$ for the [N II] 205 μm and [N II] 122 μm observations, respectively. For the Lu data, the beam size is $0''.97 \times 0''.80$.

Because different resolutions were obtained in different bands, we tried to match the resolution as much as possible. For comparison with the Lu data, we made $1''.5$ -resolution images for both Band 6 data sets to estimate the line width and the flux. For the [N II] 122 μm data, we investigated signal-to-noise ratios (S/Ns) over a few `uvtaper` parameters. We chose the `uv-tapering` parameter of $330 \text{ k}\lambda$ with the synthesized beam of $0''.44 \times 0''.38$, which is the size without losing significant S/N, i.e., peak S/N from ≈ 7.3 (7.3) to ≈ 7.1 (8.2) for the SMG (QSO). We also made highly tapered [N II] 122 μm images in order to obtain a resolution that was close to the [N II] 205 μm data. With the `uv-tapering` parameter of $80 \text{ k}\lambda$, the beam size is $1''.20 \times 1''.13$. This gives lower peak S/Ns of ~ 2 – 3 for both galaxies. In Section 4, we use the highly tapered images (“ $80 \text{ k}\lambda$ -tapered map”) to evaluate potential systematic errors. For our [N II] 205 μm data, we applied Briggs weighting with a robustness of 0.5, which gives a synthesized beam of $1''.32 \times 0''.68$. We subtracted the continuum based on image datacube using `imcontsub` to better control the continuum shape especially for targets away from the phase center and hence to get higher S/N than using `uvcontsub`. We checked that the flux measured from the data after applying `uvcontsub` gives consistent values within errors.

We measured the flux after investigating the flux growth curves with various aperture sizes. The flux values reach the asymptotic values with aperture sizes of $1''.2$ and $3''.0$ for the [N II] 122 μm and [N II] 205 μm , respectively. Using these aperture sizes, we derived the flux values based on Gaussian fitting using CASA task `imfit`.

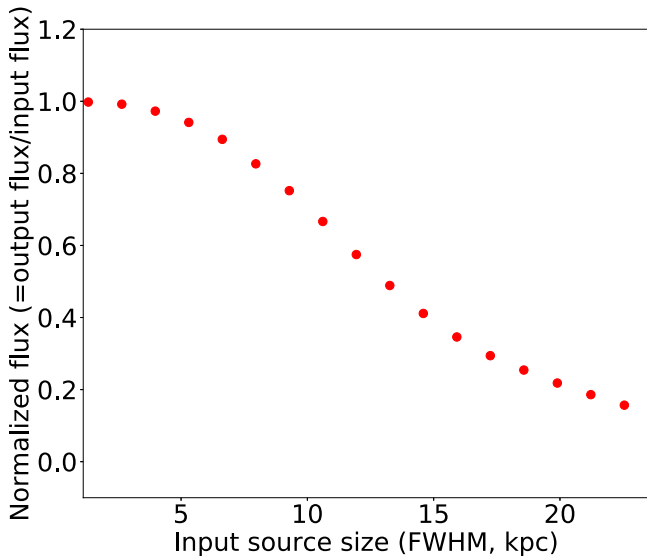


Figure 1. Expected missing flux assuming a Gaussian distribution at given flux using CASA simulation with uv -tapering of $330\text{ k}\lambda$ for an ideal case without noise.

2.5. Missing Flux

Considering the high angular resolution obtained in the [N II] $122\text{ }\mu\text{m}$ observations, we explored the possibility of emission from extended regions. We investigated mock observations of a Gaussian structure component with various sizes at given configuration of C34-5 during cycle 2 using the CASA task `simobserve`. Figure 1 shows such an experiment, when the images are created after applying the same uv -tapering parameter of $330\text{ k}\lambda$. At an ideal condition of infinity S/N (i.e., without noise), we were able to recover more than 80% of total flux when the size of the source is extended up to a size of $\approx 8\text{ kpc}$.

We estimated the sizes of [N II] emitting regions using the CASA task `imfit`. We used the natural-weight maps of the [N II] $122\text{ }\mu\text{m}$. We could only constrain the size of the QSO, which is $0''.43(\pm 0''.15) \times 0''.23(\pm 0''.18)$ and the upper limit for the SMG, which is $0''.38 \times 0''.23$. For comparison, the beam-deconvolved [N II] $205\text{ }\mu\text{m}$ sizes are $0''.59(\pm 0''.19) \times 0''.42(\pm 0''.21)$ and $0''.78(\pm 0''.18) \times 0''.62(\pm 0''.38)$ for the QSO and the SMG, respectively, from the Briggs-weighted maps. While there is a hint of smaller sizes for the [N II] 122 emissions compared to the [N II] 205 from these measurements, we note that the uncertainties are also large. At least from the Gaussian fitting, we conclude that both [N II] lines are emitted from regions of similar sizes comparable to or smaller than the [C II] emitting regions, which are $\approx 2\text{--}3\text{ kpc}$ in scale radius (Carniani et al. 2013). Lu17 reported extended emissions (i.e., $\sim 9\text{ kpc}$ ($\approx 1''.4$) for the QSO and 14 kpc ($\approx 2''.1$) for the SMG) in [N II] $205\text{ }\mu\text{m}$ line, which are larger than the estimates from our data. We could only constrain the [N II] $205\text{ }\mu\text{m}$ size for the QSO from the Lu data, $0''.81(\pm 0''.21) \times 0''.49(\pm 0''.34)$, which is consistent with our data (the size before deconvolution is $1''.21(\pm 0''.10) \times 1.00(\pm 0''.07)$). For the SMG, the size before beam deconvolution is $1''.58(\pm 0''.19) \times 0''.80(\pm 0''.06)$, but the fit gives only an upper limit of the size to be $1''.50 \times 0''.28$. It may be worth noting that our data is deeper in terms of the point source sensitivity by $1.4\times$. Considering this, it is less likely that a significant amount of emission is coming from extended

regions ($>10\text{ kpc}$). Therefore, we rely on the flux measurements without any correction.

3. Results

For the [N II] 205 line emission, we found that our measurements are consistent with the Lu data within the uncertainties, in terms of the peak positions, the line widths, and the luminosities. The spectra of all these data sets are shown in Figure 2. Pavesi et al. (2016) used our Band 6 data and reported the flux measurement briefly, which we reconfirm with the same data set but with different imaging processes. We note that Lu17 reported different flux values i.e., 0.99 ± 0.02 and 1.01 ± 0.02 for the SMG and the QSO, respectively, in which they used different aperture sizes for individual galaxies as opposed to ours. The flux values with the same flux extraction methods to ours using the Lu data are 1.07 ± 0.16 (SMG) and 0.81 ± 0.10 (QSO). These are consistent with our measurements listed in Table 1 within the errors. However, all flux values using the TDM data tend to be smaller (larger) for the SMG (QSO) compared to our data (in frequency-domain mode). While it is difficult to investigate the origin of the difference, we emphasize that we measured the line fluxes after careful analysis of the flux growth curves from Gaussian fitting and aperture photometry.

From our Band 8 observations, the [N II] $122\text{ }\mu\text{m}$ line is detected in both of the SMG and the QSO. The spectra for individual galaxies are shown in Figure 2. The line intensity maps are shown in Figure 3 with the peak positions of the [C II] line, which are consistent with each other, and the peak positions of [N II] and [C II] emissions are consistent with each other considering the S/Ns and the beam sizes.

As described in Table 1, the width of the [N II] $122\text{ }\mu\text{m}$ line for the QSO is $613 \pm 133\text{ km s}^{-1}$, which is broader roughly by a factor of two than those observed in the [N II] $205\text{ }\mu\text{m}$ line ($297 \pm 104\text{ km s}^{-1}$), [C II] ($300 \pm 28\text{ km s}^{-1}$), and CO lines ($\approx 300\text{--}350\text{ km s}^{-1}$) in the literature (e.g., Salomé et al. 2012; Carniani et al. 2013). We performed the following tests to verify whether the different line width is an effect of the different analyses. First, we did not find systematic differences in the line profile between the tapered and the natural-weight map. Second, we found that the line profile is robust regardless of continuum-subtraction methods: the continuum subtraction based on the 1D spectrum using the $0''.6$ -aperture is consistent with the `imcontsub` and `uvcontsub`. Therefore, we conclude that the different line widths between [N II] 122 and [N II] 205 for the QSO are likely real. This may indicate higher electron densities at higher velocities for the QSO, which we will discuss in the following section.

4. Discussion

We estimate the electron density using the observed ratios between two fine-structure lines of N^+ . We used the PYNEB package (Luridiana et al. 2015) to perform the calculations. The observed $122\text{ }\mu\text{m}/205\text{ }\mu\text{m}$ line luminosity ratios are 1.44 ± 0.36 and 3.89 ± 0.71 for the SMG and the QSO, respectively. These correspond to the electron densities of 26_{-11}^{+12} (SMG) and $134_{-39}^{+50}\text{ cm}^{-3}$ (QSO) at the electron temperature of $T_e = 8000\text{ K}$ (Figure 4), which is used in local spiral galaxy studies (Herrera-Camus et al. 2016).

We evaluate potential systematic errors coming from extracting the flux values in the following manner. First, using the

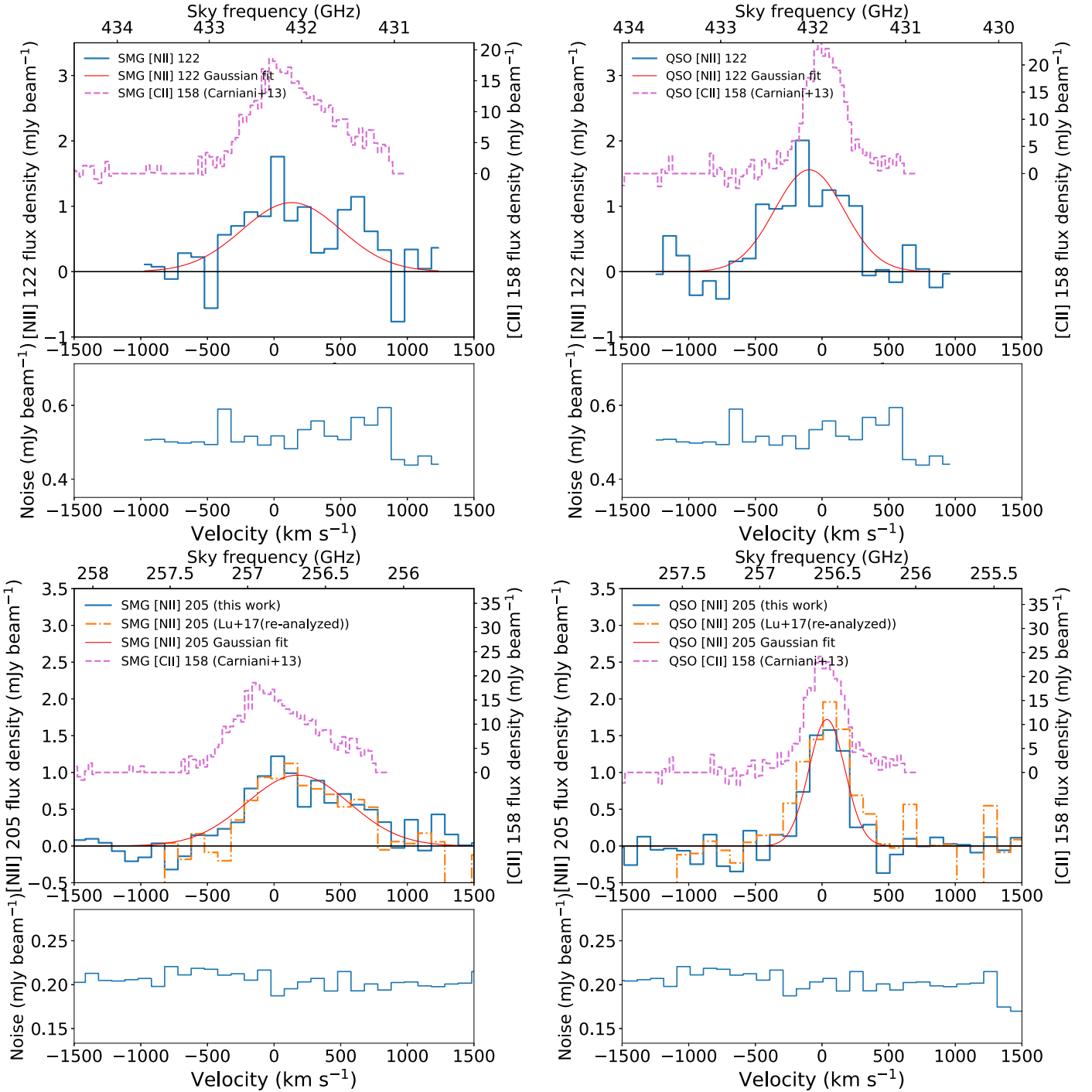


Figure 2. Detection of [N II] 122 (top row) and [N II] 205 (bottom row) lines from SMG (left panels) and QSO (right panels) in blue solid lines. Top row: the [N II] 122 spectra. The [N II] 122 μm spectrum extracted at the peak position in 100 km s^{-1} resolution from the $330 \text{ k}\lambda$ -tapered (i.e., $0''.44 \times 0''.38$) cubes. We overplot [C II] $158 \mu\text{m}$ line from Carniani et al. (2013) with the base level shifted to 1.5 for clarity. Bottom row: the [N II] 205 spectra in 100 km s^{-1} resolution. The spectra are obtained from the $1''.5 \times 1''.5$ resolution cubes at the peak positions. Overlaid orange dashed lines show the [N II] 205 μm detection from another independent data set reported in Lu17, which we re-analyzed for our comparison. We matched the resolution to $1''.5 \times 1''.5$ resolution for this data. We overplot [C II] $158 \mu\text{m}$ line from Carniani et al. (2013) with the base level shifted to 1.0 for clarity. The velocity centers of the spectra are based on the redshifts from [C II] $158 \mu\text{m}$ observations in Carilli et al. (2013).

$80 \text{ k}\lambda$ -tapering map, the [N II] 122 μm fluxes are 1.19 ± 0.49 and 1.93 ± 0.58 , for the SMG and the QSO, respectively, using the same aperture size of $3''.0$. This is consistent with the value obtained from the $330 \text{ k}\lambda$ -tapered maps measurement within errors. Second, we also measured the line fluxes using a smaller aperture size of $1''.8$ for the [N II] 205 μm data, which is determined after taking into account the emitting size of the

[N II] 122 μm line at most ($\approx 1''.2$ from the growth curve) and the [N II] 205 μm beam size. The flux values from the aperture photometry are 1.00 ± 0.07 and 0.57 ± 0.04 and Jy km s^{-1} for the SMG and the QSO, respectively, providing $n_e = 41_{-15}^{+17}$ (SMG) and $199_{-63}^{+88} \text{ cm}^{-3}$ (QSO). While these estimates give the lower limit of the electron densities when the size difference between two [N II] lines are large (i.e., the [N II] 122 μm emitting

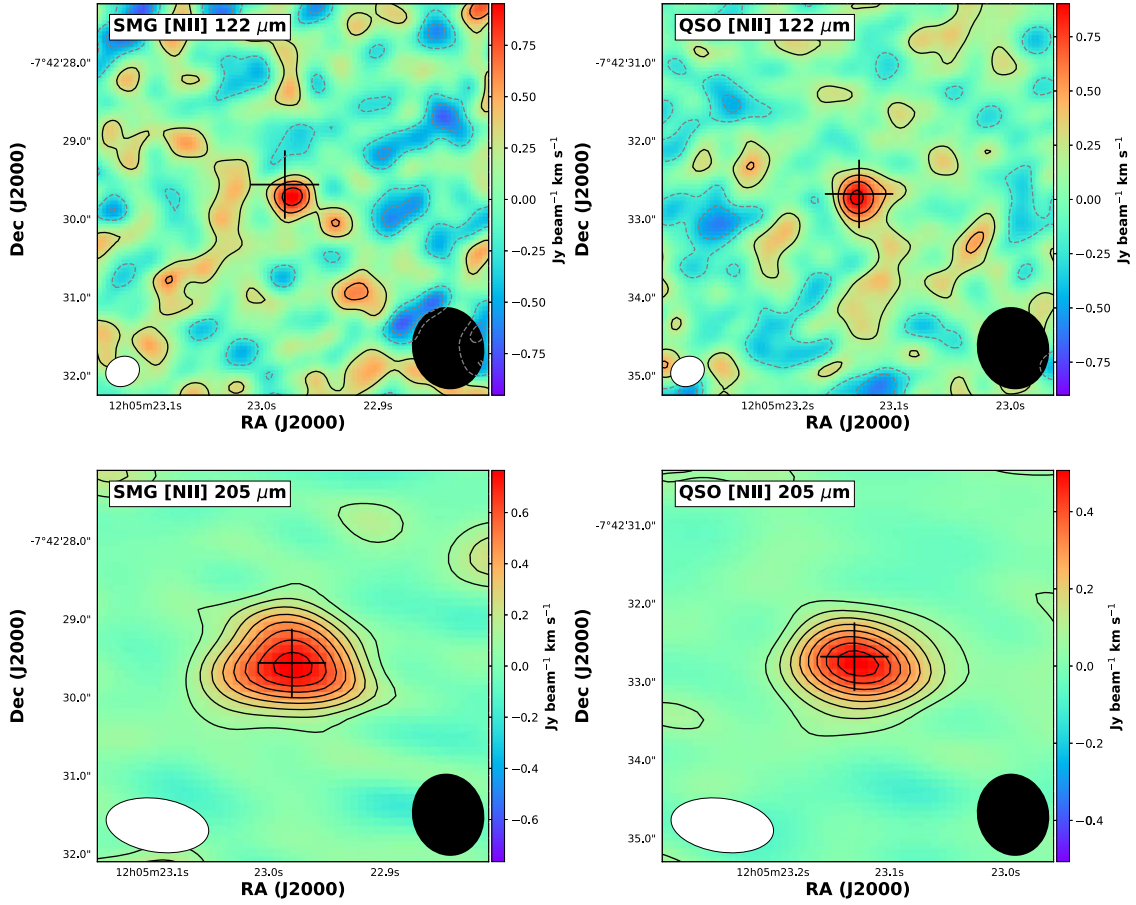


Figure 3. Top row: the line intensity of [N II] 122 μm for SMG (top-left panel) and QSO (top-right panel). Contour lines are starting from 2σ , in steps of 2σ where 1σ is 0.13 and 0.10 in Jy km s^{-1} for the SMG and the QSO, respectively. We also added negative contours of -4σ and -2σ in gray dashed lines. The beam sizes after uv -tapering are shown in white filled ellipses, which is $0''.44 \times 0''.38$. Bottom row: the line intensity of [N II] 205 μm for SMG (bottom-left panel) and QSO (bottom-right panel). Contour lines start from 2σ , in steps of 2σ where 1σ is 0.04 and 0.03 in Jy km s^{-1} for the SMG and the QSO, respectively. The beam size is $1''.32 \times 0''.68$. All panel sizes are $5''$ -width. The cross markers are the peak positions of the [C II] 158 line and the ellipse filled in black is the beam size of the [C II] observations, which is $0''.8 \times 0''.7$.

Table 1
Flux Measurements

Target	SMG			QSO		
	F_{line}^a (Jy km s^{-1}) (2)	FWHM (km s^{-1}) (3)	L_{line} ($\times 10^9 L_{\odot}$) (4)	F_{line}^a (Jy km s^{-1}) (5)	FWHM (km s^{-1}) (6)	L_{line} ($\times 10^9 L_{\odot}$) (7)
[N II] 122 μm	1.13 ± 0.27	871 ± 228	2.71 ± 0.65	1.62 ± 0.27	613 ± 133	3.89 ± 0.65
[N II] 205 μm	1.32 ± 0.11	1009 ± 147	1.86 ± 0.15	0.70 ± 0.05	297 ± 104	0.98 ± 0.07

Note.

^a We measured the flux with an aperture size of $1''.2$ and $3''.0$ for [N II] 122 μm and [N II] 205 μm , respectively.

regions being much smaller than the [N II] 205 μm emission), they serve as a gauge for the central regions. Third, if we perform 2D-Gaussian fit for the the [N II] 122 μm emission using $3''$ -aperture for the 330 k λ map, the flux values are 2.18 ± 1.01 and 1.68 ± 0.77 for the SMG and the QSO, where the uncertainties then become quite large. From these potential systematic errors, we conclude that the derived electron densities can increase up to by a factor of ~ 1.5 for the QSO and ~ 3 for the SMG.

Variation in electron densities in different galaxies have been argued in several studies. For example, Herrera-Camus et al. (2016) argued that the electron density correlates with the star

formation surface rate density for local spirals using the same [N II] tracer, based on the spatially resolved emission at $\sim \text{kpc}$ scale. Kaasinen et al. (2017), using the optical tracer of [O II] for $z \sim 1.5$ star-forming galaxies, discussed that the star formation rate (SFR) is the main driver of varying electron densities. On the other hand, Sanders et al. (2016) did not find a clear trend of electron density with SFR. We estimated the rest-frame 123 μm dust continuum (Band 8) sizes based on the uv multifit (Martí-Vidal et al. 2014), which are ≈ 1 kpc for both galaxies. Considering similar SFRs of $\approx 1000 M_{\odot} \text{yr}^{-1}$ (e.g., Salomé et al. 2012) and similar dust sizes, we do not find

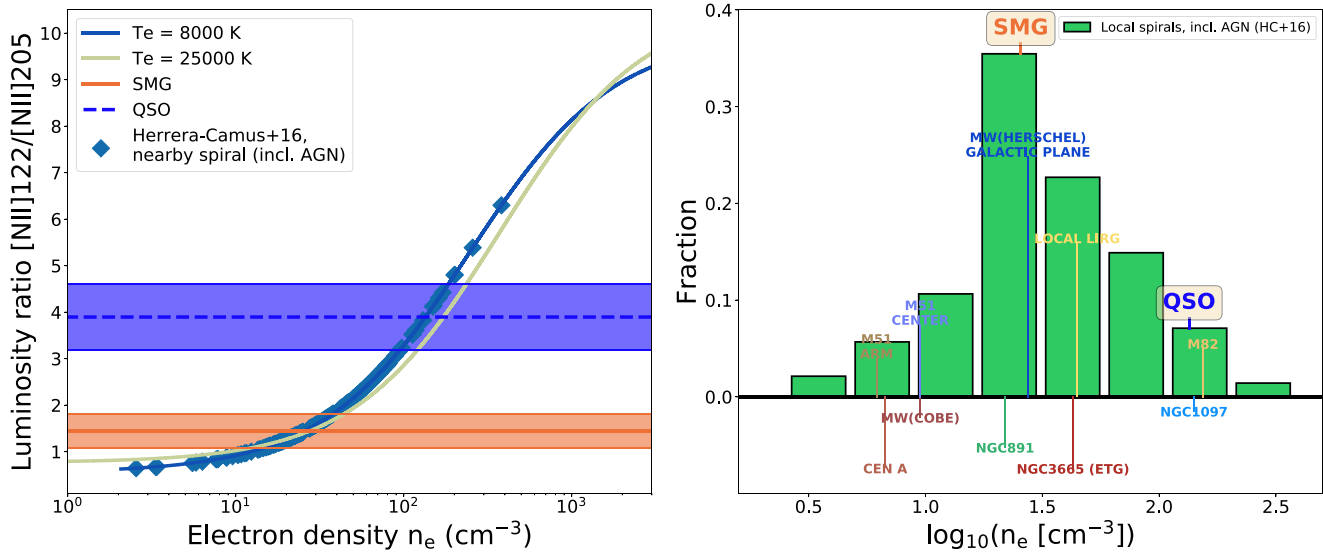


Figure 4. Left panel: the [N II] line luminosity ratio as a function of electron density. The two solid curves are for different electron temperatures ($T_e = 8000$ and $25,000$ K). The line ratios for the SMG and the QSO are shown as green solid and purple dashed lines, respectively. We also plot the observed line ratio for local populations. The line ratios obtained from local spirals (Herrera-Camus et al. 2016) are also plotted. Right panel: the histogram for the distribution of electron density, based on the observed line ratio for Herrera-Camus et al. (2016) for comparison with the BR1202–0725 system. The remaining data sets are retrieved from Bennett et al. (1994; Milky Way (MW): COBE), Goldsmith et al. (2015; MW: galactic plane), Parkin et al. (2013; M51), Petuchowski et al. (1994; M82), Parkin et al. (2014; Cen A), Hughes et al. (2015; NGC 891), Beirão et al. (2012; NGC 1097), Xiao et al. (2018; NGC 3665, early-type galaxy), and Díaz-Santos et al. (2017; local luminous infrared galaxies).

the dependence of electron density on the SFR or SFR surface density on a *global* scale.

The difference may be indicative of different phases for the black hole growth and/or different gas distributions in the SMG and the QSO. One possible scenario is that gas may be more centrally concentrated for the QSO compared to the SMG. This is counter-intuitive from the preferred formation scenario of elliptical galaxies and the connection between SMGs and QSOs (e.g., Hopkins et al. 2008; Toft 2014) where (SMG-like) heavily dust-obscured compact phase with “denser” ISM precedes the optically bright QSO phase. However, so far no conclusive argument has been made for the connection. The different [N II] line widths in the QSO might indicate higher line ratios of [N II] 122/205 in the high-velocity components, thus higher electron densities. If the above scenario is considered, this may be ascribed to gas in the core perhaps at the inner peak of the rotation curve, possibly close to the black hole. We investigated whether the line profiles are different in the center ($r < 0''.2$) and outer region ($0''.2 < r < 0''.4$). But we could not find any statistically significant difference in the fitted line widths, partially owing to the low S/N.

Alternatively, the high-density gas in the QSO may be a signature of (moderately dense) ionized outflowing gas. We note that there is a “red wing” in the [C II] line profile (Carilli et al. 2013; Carniani et al. 2013), which may be associated with a faint companion or with an outflow. Observations of active galactic nuclei-driven galactic outflows in the local universe (e.g., Sakamoto et al. 2009; Kawaguchi et al. 2018) support the idea of denser gas in the outflowing wind, perhaps due to gas compression. As it is difficult to obtain the matched resolution spectra for both galaxies owing to the sensitivity limit, future deeper high-resolution observations are needed to confirm.

For more comparison, we compiled the available data sets for various types of galaxies including our Galaxy (MW) and local galaxies as shown in Figure 4. We note that these local measurements are in most cases based on spatially resolved emissions and they have a range of electron densities within the

galaxies, while our case is for the global average value of the system, assuming that both [N II] lines are coming from the same region. The SMG has comparable electron density compared to those observed in the Galactic Plane (Goldsmith et al. 2015) and the average values of nearby, star-forming galaxies (Herrera-Camus et al. 2016) using the same tracers, even though the SFRs differ on two to three orders of magnitude. Meanwhile, the QSO shows a similar value to the starburst galaxy like M82 (Petuchowski et al. 1994) and NGC 1097 (Beirão et al. 2012). It is also similar to the typical n_e values found in the central regions of nearby galaxies (Herrera-Camus et al. 2016), which are represented by the last two bins in the electron density distribution in the right panel of Figure 4.

There are limited number of higher redshift ($z > 1$) galaxies with the [N II] line detections (e.g., Zhang et al. 2018; Novak et al. 2019). In Zhang et al. (2018), they estimated the lower limits of electron densities for lensed, dusty starbursts at a range of $z = 1\text{--}3.6$ based on stacking analysis, which is $n_e > 100 \text{ cm}^{-3}$. Given the range of electron densities in the BR1202–0725 system, the stacking analysis may have missed a portion of dusty star-forming galaxies with low electron densities like BR1202–0725 SMG. Novak et al. (2019) also reported higher lower limit of electron density ($n_e > 180 \text{ cm}^{-3}$) for a QSO at $z = 7.5$. Similarly, but using the rest-frame optical lines of [O II] and [S II], several studies reported higher electron densities on average compared to local galaxies ranging between ~ 100 and 250 cm^{-3} (e.g., Sanders et al. 2016; Kaasinen et al. 2017), but there are scatters in the measurements. It may be worth noting that these optical lines can trace slightly denser gas in the $100 < n_e/\text{cm}^{-3} < 10^4$ range compared to the [N II] lines $10 < n_e/\text{cm}^{-3} < 500$. Thus, it is likely that rest-frame optical lines n_e measurements (e.g., [O II] and [S II] lines) yield, on average, higher electron density measurements.

In this respect, there may be extremely high electron densities in central regions or elsewhere perhaps with extreme SFR densities where the [N II] lines are not viable for measuring electron densities. As seen from the resolved measurement in the local galaxies (e.g., Goldsmith et al. 2015; Herrera-Camus et al. 2016), we do not expect these galaxies to have uniform electron gas densities across the galaxy, but rather to follow some sort of distribution (e.g., a log-normal distribution like the diffuse warm ionized medium). If such is the case, the [N II]122/205 line ratio can only probe a part of the whole density distribution. Therefore, it could be that both the QSO and SMG have similar *mean* electron densities but different distribution widths, which could be the reason why the [N II]-based n_e measurement in the SMG are lower than that in the QSO. To confirm the existence of extremely high-density regime, we need other lines instead to trace such regime with higher critical density, such as [N III] or the combination of [O III]52 μm and [O III]88 μm , which can be only accessible from space telescopes.

Considering the existence of the heavily obscured galaxy such as Arp 220 and the fact that shorter wavelengths tend to be more affected by the dust, the reduction of the intrinsic value of the [N II]122/205 line ratio of the SMG compared to the QSO might be (at least partially) owing to the extremely dusty nature of the SMG. Deeper high angular resolution observations at various wavelength would confirm the true nature of the SMG and the QSO.

The success of the [N II] 122 and 205 μm detections at $z = 4.69$ demonstrate the power of future systematic surveys of extreme starbursts at $z > 4$, using these lines for probing the ISM conditions, and the effects on surrounding environments in terms of electron densities.


We deeply appreciate the anonymous referees for the fruitful discussions and suggestions for the revision of the Letter. We thank Rodrigo Herrera-Camus for providing the data set of local galaxy survey for [N II] lines and fruitful discussions. We also thank Zhi-yu Zhang for the helpful discussions on the treatment of the flux measurement. This Letter makes use of the following ALMA data: ADS/JAO.ALMA #2013.1.00259.S. ALMA is a partnership of ESO (representing its member states), NSF (USA) and NINS (Japan), together with NRC (Canada) and NSC and ASIAA (Taiwan) and KASI (Republic of Korea), in cooperation with the Republic of Chile. The Joint ALMA Observatory is operated by ESO, AUI/NRAO and NAOJ. S.C. is supported from the ERC Advanced Grant INTERSTELLAR H2020/740120. This work was supported by NAOJ ALMA Scientific Research grant Nos. 2018-09B. R.M. acknowledges ERC Advanced Grant 695671 “QUENCH.”

Facility: ALMA.

Software: astropy (Astropy Collaboration et al. 2013).

ORCID iDs

Minju M. Lee  <https://orcid.org/0000-0002-2419-3068>
 Tohru Nagao  <https://orcid.org/0000-0002-7402-5441>
 Carlos De Breuck  <https://orcid.org/0000-0002-6637-3315>
 Stefano Carniani  <https://orcid.org/0000-0002-6719-380X>
 Giovanni Cresci  <https://orcid.org/0000-0002-5281-1417>
 Bunyo Hatsukade  <https://orcid.org/0000-0001-6469-8725>
 Ryohei Kawabe  <https://orcid.org/0000-0002-8049-7525>

Kotaro Kohno  <https://orcid.org/0000-0002-4052-2394>
 Filippo Mannucci  <https://orcid.org/0000-0002-4803-2381>
 Alessandro Marconi  <https://orcid.org/0000-0002-9889-4238>
 Kouichiro Nakanishi  <https://orcid.org/0000-0002-6939-0372>
 Toshiki Saito  <https://orcid.org/0000-0002-2501-9328>
 Yoichi Tamura  <https://orcid.org/0000-0003-4807-8117>
 Hideki Umehata  <https://orcid.org/0000-0003-1937-0573>
 Min Yun  <https://orcid.org/0000-0001-7095-7543>

References

- Astropy Collaboration, Robitaille, T. P., Tollerud, E. J., et al. 2013, *A&A*, **558**, A33
- Beirão, P., Armus, L., Helou, G., et al. 2012, *ApJ*, **751**, 144
- Bennett, C. L., Fixsen, D. J., Hinshaw, G., et al. 1994, *ApJ*, **434**, 587
- Brauher, J. R., Dale, D. A., & Helou, G. 2008, *ApJS*, **178**, 280
- Carilli, C. L., Riechers, D., Walter, F., et al. 2013, *ApJ*, **763**, 120
- Carniani, S., Marconi, A., Biggs, A., et al. 2013, *A&A*, **559**, A29
- Díaz-Santos, T., Armus, L., Charmandaris, V., et al. 2017, *ApJ*, **846**, 32
- Farrah, D., Leouteiller, V., Spoon, H. W. W., et al. 2013, *ApJ*, **776**, 38
- Fontana, A., Cristiani, S., D’Odorico, S., Giallongo, E., & Savaglio, S. 1996, *MNRAS*, **279**, L27
- Goldsmith, P. F., Yıldız, U. A., Langer, W. D., & Pineda, J. L. 2015, *ApJ*, **814**, 133
- Herrera-Camus, R., Bolatto, A., Smith, J. D., et al. 2016, *ApJ*, **826**, 175
- Herrera-Camus, R., Sturm, E., Graciá-Carpio, J., et al. 2018a, *ApJ*, **861**, 94
- Herrera-Camus, R., Sturm, E., Graciá-Carpio, J., et al. 2018b, *ApJ*, **861**, 95
- Hopkins, P. F., Cox, T. J., Kereš, D., & Hernquist, L. 2008, *ApJS*, **175**, 390
- Hu, E. M., McMahon, R. G., & Egami, E. 1996, *ApJL*, **459**, L53
- Hughes, T. M., Foyle, K., Schirm, M. R. P., et al. 2015, *A&A*, **575**, A17
- Iono, D., Yun, M. S., Elvis, M., et al. 2006, *ApJL*, **645**, L97
- Isaak, K. G., McMahon, R. G., Hills, R. E., & Withington, S. 1994, *MNRAS*, **269**, L28
- Kaasinen, M., Bian, F., Groves, B., Kewley, L. J., & Gupta, A. 2017, *MNRAS*, **465**, 3220
- Kawaguchi, T., Ozaki, S., Sugai, H., et al. 2018, *PASJ*, **70**, 93
- Lord, S. D., Hollenbach, D. J., Haas, M. R., et al. 1996, *ApJ*, **465**, 703
- Lu, N., Zhao, Y., Díaz-Santos, T., et al. 2017, *ApJL*, **842**, L16
- Luridiana, V., Morisset, C., & Shaw, R. A. 2015, *A&A*, **573**, A42
- Malhotra, S., Kaufman, M. J., Hollenbach, D., et al. 2001, *ApJ*, **561**, 766
- Martí-Vidal, I., Vlemmings, W. H. T., Muller, S., & Casey, S. 2014, *A&A*, **563**, A136
- Masters, D., McCarthy, P., Siana, B., et al. 2014, *ApJ*, **785**, 153
- McMullin, J. P., Waters, B., Schiebel, D., Young, W., & Golap, K. 2007, in *ASP Conf. Ser. 376, Astronomical Data Analysis Software and Systems XVI*, ed. R. A. Shaw, F. Hill, & D. J. Bell (San Francisco, CA: ASP), **127**
- Nagao, T., Maiolino, R., De Breuck, C., et al. 2012, *A&A*, **542**, L34
- Novak, M., Banados, E., Decarli, R., et al. 2019, *ApJ*, **881**, 63
- Ohta, K., Matsumoto, T., Maihara, T., et al. 2000, *PASJ*, **52**, 557
- Ohta, K., Yamada, T., Nakanishi, K., et al. 1996, *Natur*, **382**, 426
- Omont, A., Petitjean, P., Guilloteau, S., et al. 1996, *Natur*, **382**, 428
- Parkin, T. J., Wilson, C. D., Schirm, M. R. P., et al. 2013, *ApJ*, **776**, 65
- Parkin, T. J., Wilson, C. D., Schirm, M. R. P., et al. 2014, *ApJ*, **787**, 16
- Pavesi, R., Riechers, D. A., Capak, P. L., et al. 2016, *ApJ*, **832**, 151
- Petuchowski, S. J., Bennett, C. L., Haas, M. R., et al. 1994, *ApJL*, **427**, L17
- Planck Collaboration, Ade, P. A. R., Aghanim, N., et al. 2015, *A&A*, **582**, A29
- Sakamoto, K., Aalto, S., Wilner, D. J., et al. 2009, *ApJL*, **700**, L104
- Salomé, P., Guélin, M., Downes, D., et al. 2012, *A&A*, **545**, A57
- Sanders, R. L., Shapley, A. E., Kriek, M., et al. 2016, *ApJ*, **816**, 23
- Stacey, G. J., Geis, N., Genzel, R., et al. 1991, *ApJ*, **373**, 423
- Steidel, C. C., Rudie, G. C., Strom, A. L., et al. 2014, *ApJ*, **795**, 165
- Toft, S., Smolčić, V., Magnelli, B., et al. 2014, *ApJ*, **782**, 68
- Wright, E. L., Mather, J. C., Bennett, C. L., et al. 1991, *ApJ*, **381**, 200
- Xiao, M.-Y., Zhao, Y., Gu, Q.-S., & Shi, Y. 2018, *ApJ*, **854**, 111
- Yun, M. S., Carilli, C. L., Kawabe, R., et al. 2000, *ApJ*, **528**, 171
- Zhang, Z.-Y., Ivison, R. J., George, R. D., et al. 2018, *MNRAS*, **481**, 59
- Zhao, Y., Lu, N., Xu, C. K., et al. 2013, *ApJL*, **765**, L13
- Zhao, Y., Lu, N., Xu, C. K., et al. 2016a, *ApJ*, **819**, 69
- Zhao, Y., Yan, L., & Tsai, C.-W. 2016b, *ApJ*, **824**, 146